Recent advances in atomic imaging of organic-inorganic hybrid perovskites

Mykola Telychko [a,b], Jiong Lu [a,b,*]

[a] Department of Chemistry, National University of Singapore, 3 Science Drive 3, 117543, Singapore
[b] Centre for Advanced 2D Materials (CA2DM), National University of Singapore, 6 Science Drive 2, 117546, Singapore

A R T I C L E   I N F O

A B S T R A C T

Three-dimensional organic-inorganic hybrid perovskites (OHPs) hold a great prospect for photovoltaic applications due to their outstanding electronic and optical properties. These fascinating properties of OHPs in combination with their scalable and low-cost production make OHPs promising candidates for next-generation optoelectronic devices. The ability to obtain atomistic insights into physicochemical properties of this class of materials is crucial for the future development of this field. Recent advances in various scanning probe microscopy techniques have demonstrated their extraordinary capability in real-space imaging and spectroscopic measurements of the structural and electronic properties of OHPs with atomic-precision. Moreover, these techniques can be combined with light illumination to probe the structural and optoelectronic properties of OHPs close to the real device operation conditions. The primary focus of this review is to summarize the recent progress in atomic-scale studies of OHPs towards a deep understanding of the phenomena discovered in OHPs and OHP-based optoelectronic devices.

1. Introduction

Three-dimensional organic-inorganic hybrid lead halide perovskites have evolved into one of the most active research fields because of their excellent optoelectronic properties and remarkable performance of photovoltaic devices [1–10]. Inorganic part of OHPs consists of corner-sharing MX_6 octahedrons, where M and X represent metal cation and halogen atom (e.g. Br, I, Cl) respectively (Fig. 1a). Negatively charged inorganic perovskite lattice is stabilized by positively charged organic cations (e.g. methylammonium, $CH_3NH_3^+$) residing in the inter-octahedral space. It has been demonstrated that OHPs exhibit numerous fascinating optoelectronic properties including high open-circuit voltage, high adsorption coefficient, long carrier diffusion length and efficient charge carrier transport [11–13]. Moreover, these materials can be produced at a low cost via solution-phase synthetic methods [14–16]. All these properties make OHPs as highly promising candidates for next generation optoelectronic devices.

The exceptional optoelectronic properties of OHPs partially arise from the absence of lattice defects with deep in-gap states and non-radiative trap centers [17,18]. It is theoretically predicted that most common atomic vacancies in these materials only introduce shallow in-gap states, resulting in a negligible impact onto electronic structures of OHPs [19–21]. Such a high tolerance of OHPs' electronic properties to

atomic vacancies, is attributed to peculiar bonding and antibonding nature of the conduction band and valence band states respectively. More interestingly, recent theoretical and experimental studies demonstrate that particular type of topological defects may facilitate the photovoltaic performance of OHPs [22]. For instance, domain-like structures of OHPs were predicted to induce an alternating variation of electrostatic potential across domain boundaries [23–25]. This unique potential landscape creates internal p-n junctions which facilitate the separation of photo-excited electrons and holes in OHP-based solar cells for an enhanced photovoltaic efficiency [22]. In addition, these domain boundaries are expected to serve as "highways" for the transport of the photoexcited charge carriers [22]. In fact, such domain-like structures in various OHP series have been captured using different techniques including piezo-response force microscopy (PFM) [26–29], transmission electron microscopy (TEM) [30] and X-Ray diffraction measurements [31]. Moreover, the PFM studies of OHP thin films combined with external stimuli such as mechanical stress [32] and light illumination [33], were also performed to better understand how to control the structure and properties of OHPs. It was found that ferroelastic domain-like composition of OHPs can be efficiently controlled by external mechanical stress [32]. These contents have been covered in a few recent reviews [34,35].

Apart from this, a wealth of novel chemical and physical phenomena including giant conductance hysteresis [36], ion migration [37],
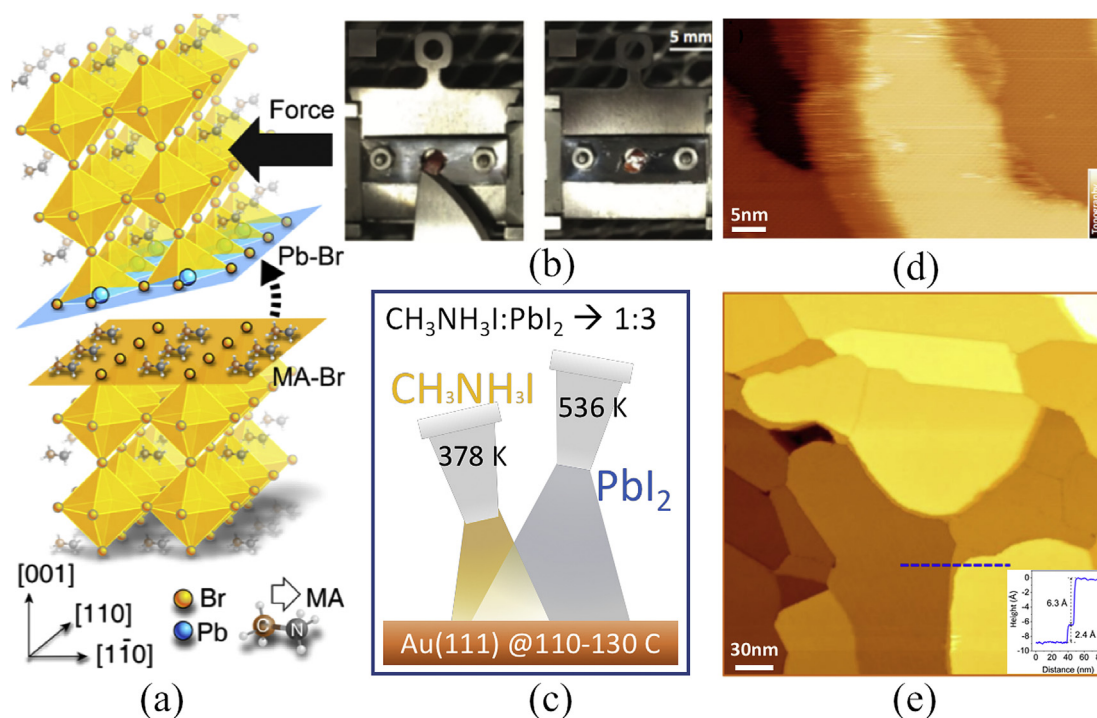
Fig. 1. Methods for the preparation of clean and flat OHPs surfaces. (a) Schematic illustration of *in-situ* cleavage of OHP crystals (with orthorhombic Miller indices) leading to two types of surface terminations, i.e., with Pb–Br and MA^+-Br^- top layers. (b) The tools for *in-situ* cleavage of OHPs used by Ohman et al. [43]. (c) Schematic illustration of the methodology of *in-situ growth of* OHP thin films involving the co-deposition of MAI and PbI_2 (1:3 ratio) on Au(111) substrate [47]. (d), (e) Representative STM images of *in-situ* cleaved $MAPbBr_3$ crystal and *in-situ* grown $MAPbI_3$ film, respectively. Inset image in (e) shows a topography profile taken along blue dashed line. Images (a), (b, d) and (e) were adapted from Refs. [43,46,47] respectively.

light-induced effects [38] or ferroelectricity [39,40] have been observed in OHPs and their devices. A deep understanding of these phenomena with unprecedented atomic insights is highly desired. It is noted that both inorganic lattice and organic cations are prone to the structural relaxation and degradation, presumably leading to a cooperative lattice distortion and varied optoelectronic properties [41,42]. It is very likely that the common characterization techniques involving light irradiation such as photoemission spectroscopy (PES) or photoluminescence (PL) measurements induce electronic excitations and structural changes of OHPs, which often make it difficult to interpret experimental results. In addition, because of the lack of atomic scale resolution, these techniques only provide sample-average information.

In contrast, the ability to gain atomic-scale understanding of all aforementioned phenomena is crucial for the fine tuning the properties of OHPs and further optimization of their device performance. Scanning tunneling microscopy (STM), transmission electron microscopy (TEM) and non-contact atomic force microscopy (ncAFM) imaging techniques offer a remarkable capability for atomically resolved imaging and spectroscopic measurements [43]. STM relies on the detection of the tunneling current flowing between atomically-sharp tip and biased OHPs, which convolutes both topography and local electronic information of the sample. Another power of STM is the ability to measure local electronic properties of the sample *via* performing scanning tunneling spectroscopy (STS). Unfortunately, it is particularly challenging to perform high resolution STM and STS measurements of air-exposed OHPs owing to their rapid surface degradation in ambient environment [44]. Such a challenge can be overcome by fabricating clean and well-defined OHP surface via *in-situ* cleavage of bulk crystals in ultra-high vacuum (UHV) conditions or *in-situ* growth of OHP thin films on conductive substrates in UHV conditions. Alternatively, TEM represents another powerful imaging technique with atomic resolution. However, OHPs are generally electron beam sensitive, posing a great challenge to acquire

atomic-resolution TEM images of OHPs [41]. Recently, Zhang and co-workers have developed a suite of methods to overcome this obstacle, which significantly advances the high resolution TEM imaging of beam-sensitive materials including OHPs [45].

Therefore, recent advances have surmounted various challenges to obtain atomically resolved imaging and spectroscopic measurements of OHPs for a better understanding of the structural and optoelectronic properties of OHPs at the atomic scale. A rapid progress in this field motivates us to review current experimental progress in the atomic-scale investigation of the structural and optoelectronic properties of OHPs by means of low-temperature STM/STS, HRTEM and nc-AFM.

1.1. Preparation of well-defined surfaces of OHPs

The seminal work by Ohman *et. al.* reports the visualization of atomic lattices of methyl-ammonium (MA^+) lead-bromide ($MAPbBr_3$), one of the most widely studied OHPs [43]. In this work, low-temperature STM/STS measurements were used to probe the atomic structure and electronic properties of $MAPbBr_3$. As illustrated in Fig. 1a-b, the authors exploited *in-situ* cleavage of single $MAPbBr_3$ bulk crystal in UHV conditions to prepare clean and atomically flat (010) surface suitable for atomically-resolved STM measurements (Fig. 1d). High-resolution STM imaging reveals a coexistence of two distinct characteristic patterns including dimer-like and zigzag-like structures (Fig. 2), which will be further discussed in later section.

Alternatively, *in-situ* growth of OHP thin films in UHV conditions serves as another approach for the preparation of the atomically-clean OHPs surface suitable for STM studies [48]. L. She *et. al.* exploited this method to fabricate $MAPbI_3$ films on Au(111) surface for atomically-resolved STM imaging [47]. As illustrated in Fig. 1c, this methodology involves a simultaneous deposition of MAI and PbI_2 precursors with a well-controlled ratio onto clean Au(111) surface kept at
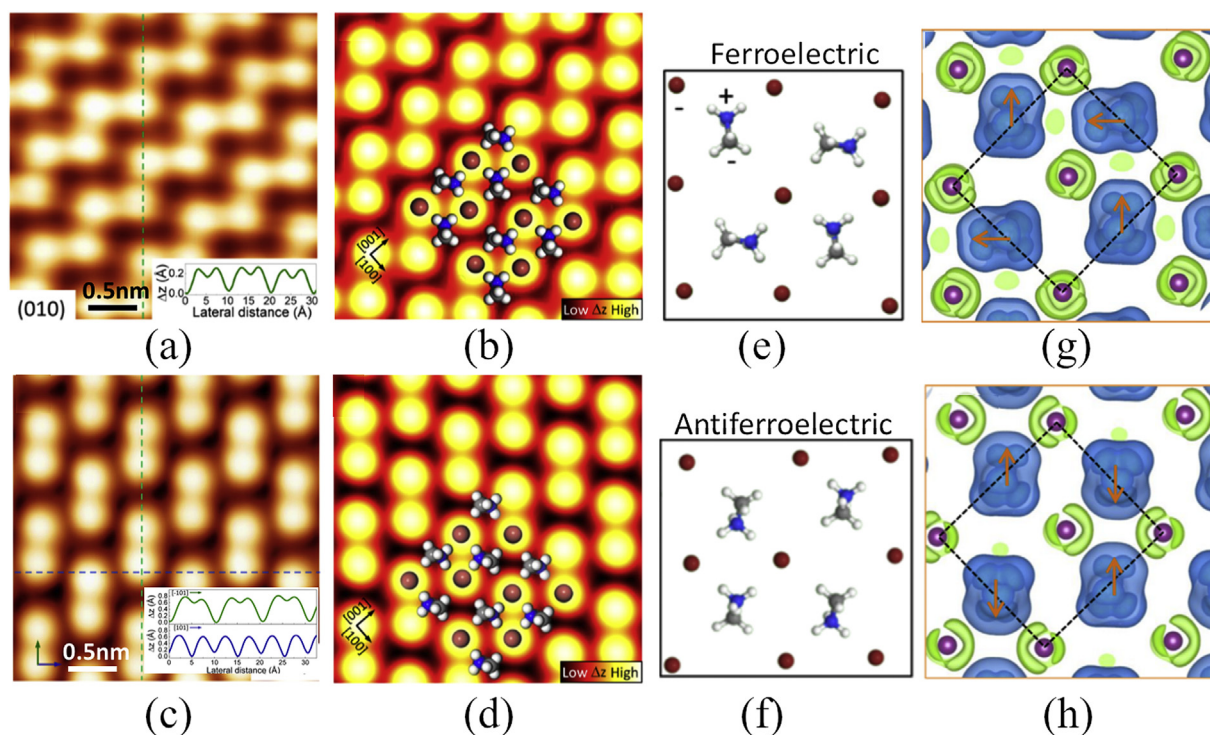
Fig. 2. Atomically resolved STM images of OHP and the physical origin of surface reconstruction. Atomically resolved STM topography images of the OHP surface and simulated STM images of the (010) plane of the orthorhombic crystal with (a, b) dimer-like and (c, d) zigzag-like pattern. Scan parameters: V = −5 V and I = 0.1 nA. The Br⁻ and MA⁺ ions are overlaid. Color code: N (blue), C (gray), H (white), Br (brown). (e, f) Atomic models showing the net ferroelectric and antiferroelectric alignment of MA⁺ dipoles. (g, h) Deformation charge density of halide-terminated OHP (001) surface of (g) zigzag and (h) dimer structure. The isosurfaces of positive and negative values ($\pm 0.02 e/\text{Å}^3$) are shown in blue and green colors, respectively. The dipole orientation of MA⁺ cations is denoted by brown arrows. Images (e-f) and (g, h) were adapted from Refs. [43,47], respectively.

elevated temperature. The subsequent STM imaging of as-prepared MAPbI₃ film resolves both zigzag and dimer patterns associated with the characteristic surface reconstructions, similar to what have been observed on *in-situ* cleaved MAPbBr₃ crystal by R. Ohman et al. [43]. Moreover, the zigzag and dimer phases can be occasionally inter-converted into each other triggered by the tunneling current during STM imaging. A detailed study reveals that the formation of MAPbI₃ thin films follows a MA-I layer by Pb–I layer growth mode, which is energetically reinforced by a completion of the [PbI]₆ octahedra [49].

1.2. Probing the orientation of MA+dipoles and origin of the surface reconstruction

Aforementioned dimer-like or zigzag-like patterns were resolved by the STM imaging of both *is-situ* cleaved OHP crystals and *in-situ* grown OHP films. Notably, both patterns are formed by the topmost halide anions, but with different inter-halide distances. For example, individual dimer is comprised by a pair of proximal Br anions located at apices of neighboring [PbBr]₆ octahedra (Fig. 2c), while zigzag pattern is formed by the reorganization of surface Br atoms into zigzag-like chains (Fig. 2 a).

The origin of these two reconstructions was interpreted by distinct orientations of interior MA⁺ cations. Fig. 2e and f depict two scenarios for the alignment of polar MA⁺ chains with a ferroelectric or antiferro-electric polarization. In addition, the attractive electrostatic interaction between positively charged MA⁺ cations and negatively charged halide atoms (Fig. 2 g, h) is expected to drive the structural relaxation of halide atoms. As shown in Fig. 2b and d, theoretical calculations and STM simulations reveal that ferroelectric orientation of MA⁺ cations in the zigzag structure results in a nonzero net dipole moment. In contrast, the antiferroelectric arrangement of MA⁺ cations produces the dimer-like

STM pattern. Note that individual dimer is formed in proximity to nearest methyl groups of MA⁺ cations. Such an interpretation of the origin of the STM contrast in both zigzag and dimer patterns was further confirmed by Y. Liu et al. [50]. Moreover, recent theoretical studies provide further evidence to support that the rotation MA⁺ cations is concomitated by the distortions of the [PbI]⁻ framework attributed to the structural relaxation observed by STM imaging [51].

1.3. The structural changes of OHPs upon light illumination

Understanding the dynamics of structural variations of OHPs under light illumination is of both fundamental and practical importance [38]. The PFM imaging with sub-micrometer resolution demonstrated that OHP develops ferroelastic domain-like composition upon light illumination [33]. Recently, H. Hsu *et. al.* [46] reported a seminal work on atomically-resolved STM study of the *in-situ* cleaved MAPbBr₃ crystals in both dark and illuminated conditions. In dark conditions, the Br-terminated surface exhibits dominant dimer patterns with a 2 × 2 unit cell, comprised by Br dimers oriented in [110] direction, which coexist with zigzag patterns comprised by Br rows along the [100] direction (Fig. 3a). The dimer and zigzag patterns are highlighted by orange and green colors respectively in Fig. 3a. However, the surface underwent dramatic change under laser illumination (532 nm), as shown in Fig. 3d. Light illumination induces the formation of new structures with a distinct periodicity (a 4 × 2 unit cell). Interestingly, the structural transition is fully reversible upon turning off the light exposure. This underpins a reversible light-induced rearrangements of MA⁺ chains and possible concomitant alternations of Br–Br distances. A thorough analysis of characteristic Br–Br distances supported by STM simulations (Fig. 3b, e) allows to derive MA⁺ dipole alignment for the pristine and illuminated surface as shown in Fig. 3c and f, respectively. The dimer pattern of
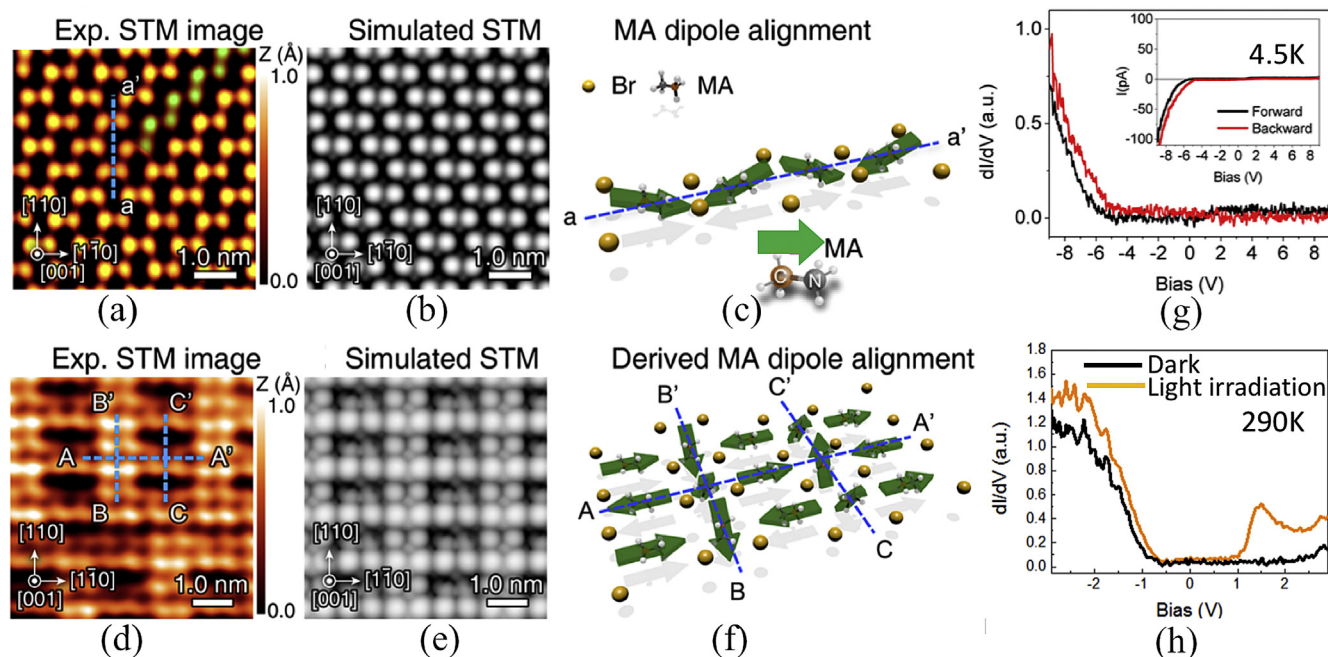
Fig. 3. STM imaging of pristine and light-illuminated MAPbBr₃. (a-f) Experimental STM image, simulated STM image and schematic illustration of MA⁺ orientation in the (a-c) dark and (d-f) under illumination. STM images of MAPbBr₃ reveal a transition from (a) the dominant dimer structure in dark to (d) a new structure with a 4 × 2 unit cell under laser illumination (532 nm). Simulated STM images of MAPbBr₃ (b) in dark and (e) under laser illumination are derived from the dipole realignments of MA⁺ molecule as shown schematically in (c) and (f) under dark and illuminated conditions, respectively. (g) STS spectra of MAPbBr₃ crystal collected at 4.5K. (h) STS spectra of MAPbBr₃ collected at room temperature in dark (black curve) and illuminated conditions (orange curve) . Images (g, h) and (a-f) were adapted from Refs. [43,46].

pristine surface arises due to the antiferroelectric alignment of MA⁺ chains. The BrBr dimer pair is formed close to the nearest positively charged ammonium groups. This interpretation is consistent with the one proposed by R. Ohman *et. al.* [43]. In contrast, MA⁺ dipoles undergo a consecutive 90° rotation along A-A' direction in the illuminated sample as shown schematically in Fig. 3f. The overall arrangement of MA⁺ cations in the illuminated sample retains the antiferroelectric alignment. As a result, one-dimensional potential energy landscape associated to light-induced anisotropic MA⁺ alignment is formed to facilitate the charge separation in the OHPs-based devices.

The plausible physical origin for the light-induced rearrangement of MA⁺ cations involves the electrostatic Coulomb interaction between Br anions and MA⁺ cations. In particular, the light illumination induces the electron excitation from valence band formed by Pb 6s and Br 5p orbitals to conduction band contributed from Pb 6p states. The charge transfer between valence band and conduction band orbitals with distinct spatial geometry creates a local polarization field within a unit cell. As a result, MA⁺ cations undergo the further rotational rearrangement in order to counteract this polarization field [46].

Previously, Ohman et al. performed STS measurements of the same MAPbI₃ crystal at low temperature (4.5 K) and room temperature under both dark and illuminated conditions as shown in Fig. 3g, h. STS spectra collected at low temperature only exhibit an appreciable dI/dV signal at negative sample bias voltage ($V_S < -5$ V) (Fig. 3g). In contrast, the STS spectra collected at room temperature exhibit a substantial dI/dV intensity at both voltage polarities. Such a dramatic difference can be attributed to the different electronic structures of cubic phase at room temperature and orthorhombic phase at low temperature [52]. Moreover, the room temperature STS spectra also reveal a reduction of band gap upon light illumination (orange curve in Fig. 3h). A decrease of band gap was also observed for MAPbI₃ thin films grown on TiO₂ substrate upon light irradiation [53], which may be associated with the reordering of MA⁺ cations or the activation of additional tunneling channels via

light irradiation [31].

1.4. Probing atomic defects and impurities

It is found that the electronic properties of OHPs are tolerant to presence of various structural defects including halide vacancies, impurities or dislocations [19]. Typically, the common defects with shallow in-gap states are strongly localized [20]. On one hand, it was demonstrated that a controllable incorporation of homovalent (e.g. Mn or Bi) atoms into the OHP lattice can be exploited for fine tuning the optoelectronic properties of OHPs [54–57]. On the other hand, it was also predicted that water or oxygen molecules tend to adsorb over the halide vacancies attributed to the rapid degradation of OHPs at ambient conditions [50]. In this regard, STM measurements not only enable a direct visualization of individual impurities and vacancies at the atomic scale, but also facilitate to unveil the electronic properties of these defects and their impact on the chemical stability of OHPs.

Fig. 4a shows the high-resolution STM imaging of OHP surface with atomic defects. The characteristic depressions are presumably attributed to Br vacancies and double Br-MA vacancies. A good agreement between the simulated STM image and experimental one further supports this structural assignment (Fig. 4b). It was theoretically predicted that these types of vacancies are the most abundant defects on the OHP surface because of their relatively low formation energies [50].

Very recently, STM was employed to resolve individual dopants introduced into the OHP lattice. Hieulle et al. used *in-situ* thin film growth technique for the fabrication of MAPbBr₃, mixed-halide MAPbBr₃₋yIy, and MAPbBr₃₋zClz thin films [58]. A post-deposition of PbI₂ (PbCl₂) compounds onto as-grown MAPbBr₃ films results in the random substitution of Br atoms by I (Cl) atoms towards the formation of mixed-halide MAPbBr₃₋yIy (MAPbBr₃₋zClz) thin films. STM imaging resolves distinct features associated with I (protrusions) and Cl (depressions) impurities, respectively. The distinct topographic STM contrast for I (Cl)
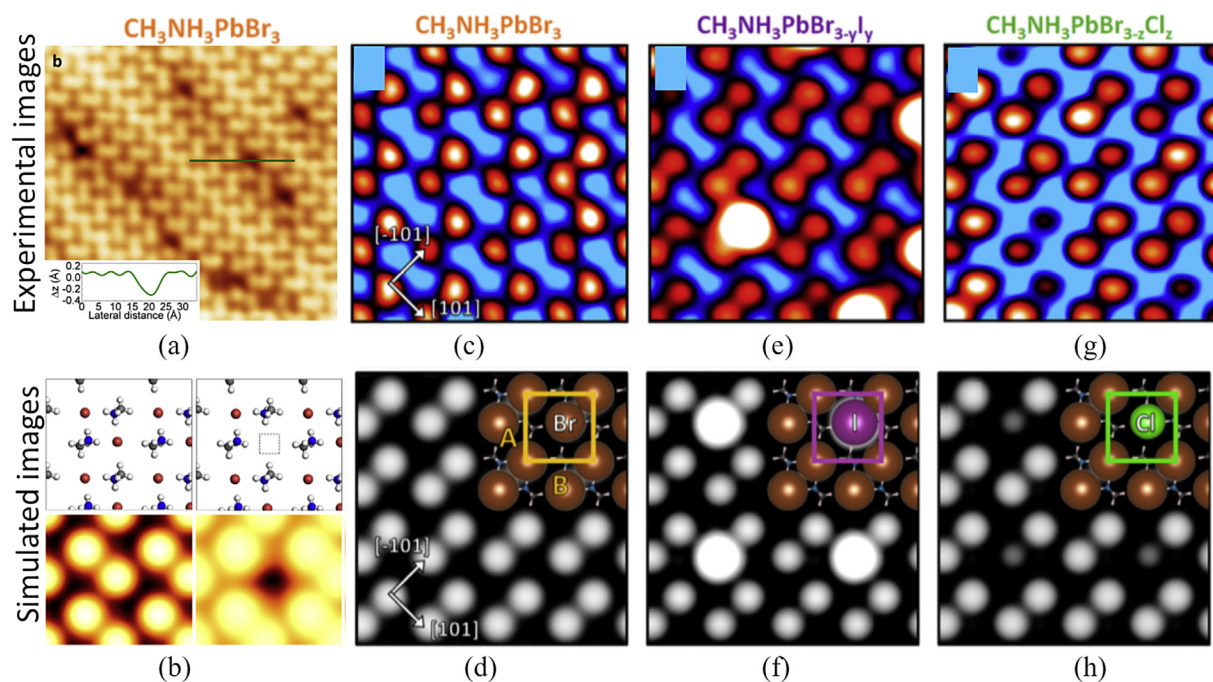
Fig. 4. STM study of defects and impurities on the OHP surface. (a) STM imaging resolves the atomic defects on the OHP surface. (b) The top layer atoms with the simulated STM images of pristine OHP (left) and halide vacancy (right). (c−g) STM images of (c) MAPbBr$_3$, (b) MAPbBr$_{3-y}$I$_y$, and (c) MAPbBr$_{3-z}$Cl$_z$ OHP surfaces. (d−h) Calculated (010) surface of the mixed-halide organic−inorganic perovskites. Images (a), (b) and (c-h) were adapted from Refs. [43,50,58].

substitutions was attributed to a larger (smaller) ionic radius in comparison to Br atom [58].

Incorporation of substitutional Cl dopant also has a profound impact on chemical and physical properties of MAPbBr$_3$ film. It is found that Cl doping results in a noticeable decrease of the surface work function by 0.2 eV (from 4.77 eV to 4.57 eV) due to a change of the surface dipole. In contrast, incorporation of substitutional I dopant shows a rather negligible modification of the surface work function of MAPbBr$_3$ (4.79 eV) due to a smaller variation of surface dipole arising from a low electronegativity of I compared to Cl. In addition, an incorporation of 12–18% of Cl atoms leads to a substantial increase of the stability of OHPs based photovoltaic devices. Murali et al. also applied *in-situ* cleavage technique to study the degradation of MAPbBr$_3$ when exposed to air [59]. Atomically-resolved STM image reveals the features associated with the formation of surface hydrate. One can envisage that future STM studies of *in-situ* cleaved OHP surface upon the dosage of target molecules (e.g. water or oxygen) in UHV conditions may provide new insights into the degradation mechanism of OHPs.

### 1.5. Transmission electron microscopy imaging of OHPs

The ionic nature of OHP lattice makes it prone to the degradation under high-energy electron beam during TEM imaging. Recently, M. Rothmann et al. used TEM to resolve the twin-like domain structures in the tetragonal MAPbI$_3$ thin film [30]. Moreover, authors demonstrated a reversible formation of domains upon cooling below threshold temperature, which is attributed to the transition from cubic to tetragonal phase [30]. Zhang *et. al.* has developed a suite of methods involving a sophisticated algorithm for efficient crystal alignment. This allows to acquire atomically-resolved TEM imaging of MAPbBr$_3$ due to a significant reduction of the electron dose (Fig. 5). HRTEM imaging unambiguously reveals distinct domain structures consisting of in-plane (Fig. 5b) and out-of-plane (Fig. 5c) orientations of the MA$^+$ dipoles, which suggests the presence of nanoscale ferroelectric order in this OHP sample. This result underpins the advantage of TEM imaging as

compared to STM imaging, since the latter does not allow to directly probe the inner MA$^+$ cations.

1.6. Non-contact atomic force microscopy study (ncAFM) of the two-dimensional OHPs

To date, nc-AFM studies have been performed only for two-dimensional (2D) OHPs, so-called Ruddlesden–Popper perovskites (RPPs) [60]. The 2D RPP perovskites can be regarded as *n* layers of inorganic octahedral sheets sandwiched by two layers of large organic spacer cations (e.g. butylammonium, CH$_3$(CH$_2$)$_3$NH$_3$, BA$^+$). This gives rise to natural multiple-quantum-well structures, in which the inorganic slabs serve as the potential "wells" while the organic layers function as the potential "barriers" [61]. Recently, K. Leng *et. al.* reported a seminal work on the visualization of the n=4 RPP (BA$_2$MA$_{n-1}$Pb$_n$I$_{3n+1}$) using nc-AFM with a Q-plus sensor [42]. Nc-AFM image of n=4 RPP reveals a square-like lattice (Fig. 6a). The bright dot in the image is expected to originate from the organic BA$^+$ cations, while interior inorganic [PbI]$^-$ lattice cannot be directly resolved. Furthermore, authors captured the emergence of the zigzag domains after thermal annealing at 60 °C (Fig. 6b). Annealing at higher temperature (90 °C) results in further development of zigzag domains (Fig. 6c). The formation of these zigzag domains was attributed to the structural relaxation of on-surface BA$^+$ chains. Interestingly, a reversible interconversion between zigzag and square patterns can be triggered by tuning the tip-sample interactions (Fig. 6d-e). Such a contrast reversal is most likely due to the tip-induced rearrangement of BA$^+$ cations. Recent advances have demonstrated an outstanding capability of the tip-functionalized nc-AFM to unveil the detailed chemical structure and charge potential in different systems with a sub-angstrom resolution [62,63]. Therefore, we believe that nc-AFM imaging of OPHs with a functionalized probe (e.g. CO or oxygen-terminated Cu tip) may provide "sub-angstrom scale" insights into the structural and electronic properties of both 2D and 3D hybrid perovskites. Furthermore, such a functionalized tip may further enhance the spatial resolution of kelvin probe force microscopy to map out the
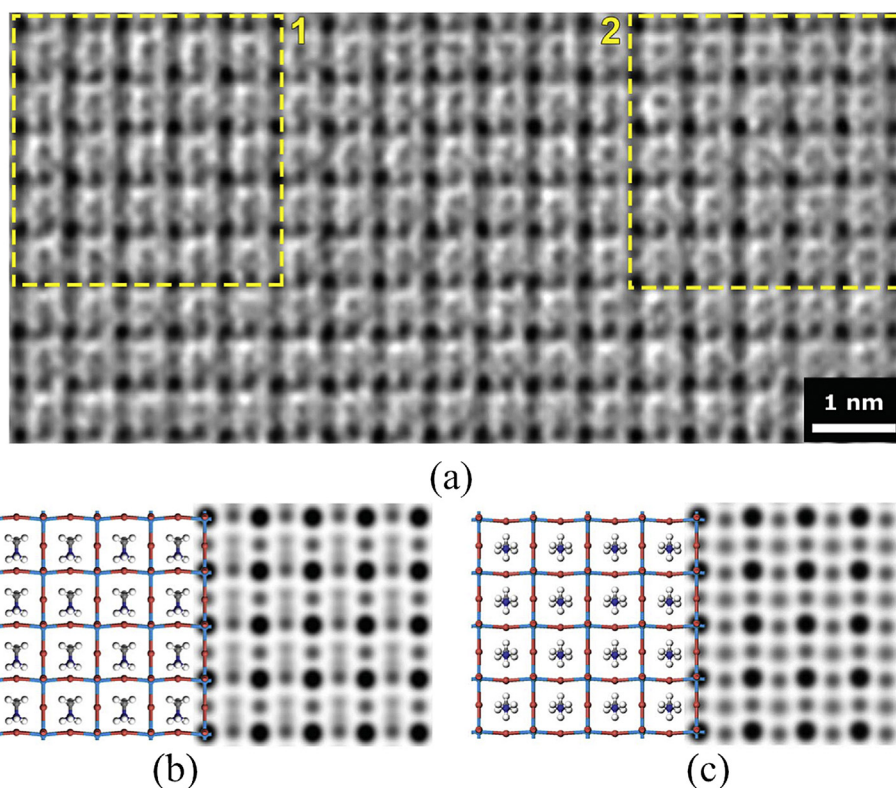
Fig. 5. HRTEM imaging of OHPs. (a) High-resolution TEM image of MAPbBr$_3$ OHP crystal. The yellow squares highlight two domain structures with different orientation of MA$^+$ cations. (b) and (c) The structural model (left) and the simulated projected potential map (right) of MAPbBr$_3$ with different MA$^+$ orientations, corresponding to region 1 and 2 in (a), respectively. Image was adapted from Ref. [45].
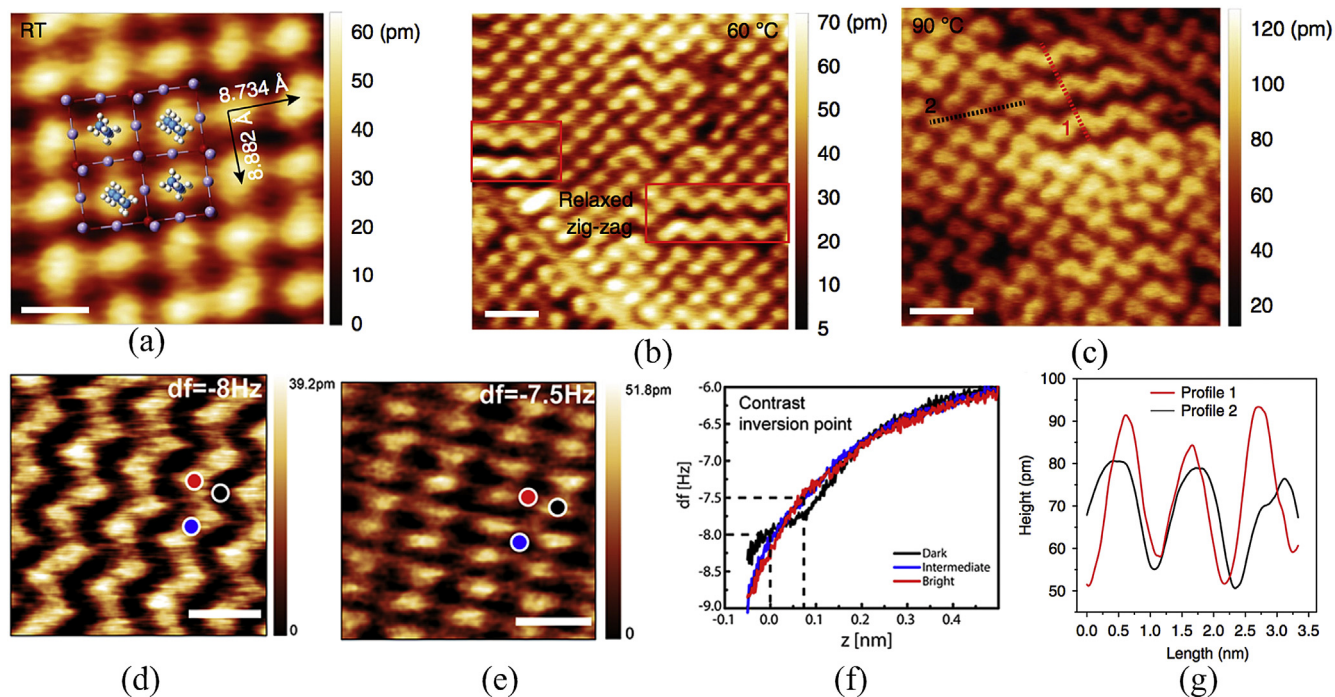
Fig. 6. Nc-AFM imaging of n=4 and n=1 Ruddlesden–Popper OHPs. (a) nc-AFM image of the initial state of the surface of n=4 BA$_2$MA$_{n-1}$Pb$_n$I3$_{n+1}$ RPP crystal. The overlapped sketch displays the top view of four unit cells of the n = 4 RPP OHP. Scale bar is 1 nm for all images. The sample is heated up to (b) 60 °C and (c), 90 °C. (d, e) nc-AFM image of n=1 BA$_2$MA$_{n-1}$Pb$_n$I3$_{n+1}$ measured at the set point of (d) the frequency shift, df=−8 Hz and (e) df=−7.5 Hz. Red, blue and black circles indicate the position where each df(z) curve was collected. Scale bar in all images is 1 nm. (f) Frequency shift versus distance (df(z)) curves taken over positions marked by circles in nc-AFM images (d, e). (g) Cross-sectional profile taken along the lines (1, 2) in panel (c). Image was adapted from Ref. [42].

local potential variation across domain walls and step edges of hybrid perovskites [53,64].

2. Conclusions and outlook

Real-space imaging of atomic structures of OHPs can be achieved using different techniques including STM, AFM and TEM. It has been demonstrated that STM imaging in combination with the external stimuli, e.g. light irradiation, enables the investigation of an instantaneous structural variation of OHPs close to the real device operation conditions. We therefore envisage that atomically-resolved studies empowered by external stimuli including mechanical stress, light illumination or exposure to ambient atmosphere, will shed new light on the puzzling OHPs phenomena such as ion migration, giant hysteresis and degradation mechanism. We also foresee that nc-AFM imaging of OPHs with a functionalized probe may provide deep insights into the structural and electronic properties of both 2D and 3D OHPs at the sub-angstrom scale. Atomic insights obtained from these studies will deepen the understanding of the mesoscopic-scale phenomena of OHPs for the further optimization of their device performance.

Acknowledgements

References

[1] M.A. Green, A. Ho-Baillie, H.J. Snaith, The emergence of perovskite solar cells, Nat. Photonics 8 (2014) 506.

[2] Y. Zhao, K. Zhu, Organic–inorganic hybrid lead halide perovskites for optoelectronic and electronic applications, Chem. Soc. Rev. 45 (2016) 655–689.

[3] P. Gao, M. Grätzel, M.K. Nazeeruddin, Organohalide lead perovskites for photovoltaic applications, Energy Environ. Sci. 7 (2014) 2448–2463.

[4] Y. Wang, S. Bai, L. Cheng, N. Wang, J. Wang, F. Gao, W. Huang, High-efficiency flexible solar cells based on organometal halide perovskites, Adv. Mater. 28 (22) (2016) 4532–4540.

[5] C. Zuo, H.J. Bolink, H. Han, J. Huang, D. Cahen, L. Ding, Advances in perovskite solar cells, Adv. Sci. 3 (7) (2016) 1500324.

[6] J.-W. Xiao, L. Liu, D. Zhang, N. De Marco, J.-W. Lee, O. Lin, Q. Chen, Y. Yang, The emergence of the mixed perovskites and their applications as solar cells, Adv. Energy Mater. 7 (20) (2017) 1700491.

[7] H. Zhu, Y. Fu, F. Meng, X. Wu, Z. Gong, Q. Ding, M.V. Gustafsson, M.T. Trinh, S. Jin, X.-Y. Zhu, Lead halide perovskite nanowire lasers with low lasing thresholds and high quality factors, Nat. Mater. 14 (2015) 636.

[8] A. Kojima, K. Teshima, Y. Shirai, T. Miyasaka, Organometal halide perovskites as visible-light sensitizers for photovoltaic cells, J. Am. Chem. Soc. 131 (17) (2009) 6050–6051.

[9] M.M. Lee, J. Teuscher, T. Miyasaka, T.N. Murakami, H.J. Snaith, Efficient hybrid solar cells based on meso-superstructured organometal halide perovskites, Science 338 (6107) (2012) 643–647.

[10] B. Saparov, D.B. Mitzi, Organic–inorganic perovskites: structural versatility for functional materials design, Chem. Rev. 116 (7) (2016) 4558–4596.

[11] A. Miyata, A. Mitioglu, P. Plochocka, O. Portugall, J.T.-W. Wang, S.D. Stranks, H.J. Snaith, R.J. Nicholas, Direct measurement of the exciton binding energy and effective masses for charge carriers in organic–inorganic tri-halide perovskites, Nat. Phys. 11 (2015) 582.

[12] J. Huang, Y. Yuan, Y. Shao, Y. Yan, Understanding the physical properties of hybrid perovskites for photovoltaic applications, Nat. Rev. Mater. 2 (2017) 17042.

[13] D. Shi, V. Adinolfi, R. Comin, M. Yuan, E. Alarousu, A. Buin, Y. Chen, S. Hoogland, A. Rothenberger, K. Katsiev, Y. Losovyj, X. Zhang, P.A. Dowben, O.F. Mohammed, E.H. Sargent, O.M. Bakr, Low trap-state density and long carrier diffusion in organolead trihalide perovskite single crystals, Science 347 (6221) (2015) 519–522.

[14] G. Xing, N. Mathews, S.S. Lim, N. Yantara, X. Liu, D. Sabba, M. Grätzel, S. Mhaisalkar, T.C. Sum, Low-temperature solution-processed wavelength- tunable perovskites for lasing, Nat. Mater. 13 (2014) 476.

[15] J. Burschka, N. Pellet, S.-J. Moon, R. Humphry-Baker, P. Gao, M.K. Nazeeruddin, M. Grätzel, Sequential deposition as a route to high- performance perovskite-sensitized solar cells, Nature 499 (2013) 316.

[16] Z. Li, T.R. Klein, D.H. Kim, M. Yang, J.J. Berry, M.F.A.M. van Hest, K. Zhu, Scalable fabrication of perovskite solar cells, Nat. Rev. Mater. 3 (2018) 18017.

[17] M. Pandey, K.W. Jacobsen, K.S. Thygesen, Band gap tuning and defect tolerance of atomically thin two-dimensional organic–inorganic halide perovskites, J. Phys. Chem. Lett. 7 (21) (2016) 4346–4352.

[18] J. Kang, L.-W. Wang, High defect tolerance in lead halide perovskite $CsPbBr_3$, J. Phys. Chem. Lett. 8 (2) (2017) 489–493.

[19] J.M. Ball, A. Petrozza, Defects in perovskite-halides and their effects in solar cells, Nat. Energy 1 (2016) 16149.

[20] F. Wang, S. Bai, W. Tress, A. Hagfeldt, F. Gao, Defects engineering for high-performance perovskite solar cells, npj Flex. Electron. 2 (1), 2018(22)

[21] D. Meggiolaro, E. Mosconi, F. De Angelis, Formation of surface defects dominates ion migration in lead-halide perovskites, ACS Energy Lett. 4 (3) (2019) 779–785.

[22] J.M. Frost, K.T. Butler, F. Brivio, C.H. Hendon, M. van Schilfgaarde, A. Walsh, Atomistic origins of high-performance in hybrid halide perovskite solar cells, Nano Lett. 14 (5) (2014) 2584–2590.

[23] S. Liu, F. Zheng, N.Z. Koocher, H. Takenaka, F. Wang, A.M. Rappe, Ferroelectric domain wall induced band gap reduction and charge separation in organometal halide perovskites, J. Phys. Chem. Lett. 6 (4) (2015) 693–699.

[24] A.R. Warwick, J. Íñiguez, P.D. Haynes, N.C. Bristowe, First-principles study of ferroelastic twins in halide perovskites, J. Phys. Chem. Lett. 10 (6) (2019) 1416–1421.

[25] L. Chen, C. Paillard, H.J. Zhao, J. Íñiguez, Y. Yang, L. Bellaiche, Tailoring properties of hybrid perovskites by domain-width engineering with charged walls, npj Comput. Mater. 4 (1) (2018) 75.

[26] I.M. Hermes, S.A. Bretschneider, V.W. Bergmann, D. Li, A. Klasen, J. Mars, W. Tremel, F. Laquai, H.-J. Butt, M. Mezger, R. Berger, B.J. Rodriguez, S.A.L. Weber, Ferroelastic fingerprints in methylammonium lead iodide perovskite, J. Phys. Chem. C 120 (10) (2016) 5724–5731.

[27] Y. Kutes, L. Ye, Y. Zhou, S. Pang, B.D. Huey, N.P. Padture, Direct observation of ferroelectric domains in solution-processed $CH_3NH_3PbI_3$ perovskite thin films, J. Phys. Chem. Lett. 5 (19) (2014) 3335–3339.

[28] H. Röhm, T. Leonhard, M.J. Hoffmann, A. Colsmann, Ferroelectric domains in methylammonium lead iodide perovskite thin-films, Energy Environ. Sci. 10 (2017) 950–955.

[29] Y. Liu, L. Collins, R. Proksch, S. Kim, B.R. Watson, B. Doughty, T.R. Calhoun, M. Ahmadi, A.V. Ievlev, S. Jesse, S.T. Retterer, A. Belianinov, K. Xiao, J. Huang, B.G. Sumpter, S.V. Kalinin, B. Hu, O.S. Ovchinnikova, Chemical nature of ferroelastic twin domains in $CH_3NH_3PbI_3$ perovskite, Nat. Mater. 17 (11) (2018).

[30] M.U. Rothmann, W. Li, Y. Zhu, U. Bach, L. Spiccia, J. Etheridge, Y.-B. Cheng, Direct observation of intrinsic twin domains in tetragonal $CH_3NH_3PbI_3$, Nat. Commun. 8 (2017) 14547.

[31] F. Bertolotti, L. Protesescu, M.V. Kovalenko, S. Yakunin, A. Cervellino, S.J.L. Billinge, M.W. Terban, J.S. Pedersen, N. Masciocchi, A. Guagliardi, Coherent nanotwins and dynamic disorder in cesium lead halide perovskite nanocrystals, ACS Nano 11 (4) (2017) 3819–3831.

[32] E. Strelcov, Q. Dong, T. Li, J. Chae, Y. Shao, Y. Deng, A. Gruverman, J. Huang, A. Centrone, $CH_3NH_3PbI_3$ perovskites: ferroelasticity revealed, Sci. Adv. 3 (4) (2017).

[33] D. Kim, J.S. Yun, P. Sharma, D.S. Lee, J. Kim, A.M. Soufiani, S. Huang, M.A. Green, A.W.Y. Ho-Baillie, J. Seidel, Light- and bias-induced structural variations in metal halide perovskites, Nat. Commun. 10 (1) (2019) 444.

[34] J. Hieulle, C. Stecker, R. Ohmann, L.K. Ono, Y. Qi, Scanning probe microscopy applied to organic–inorganic halide perovskite materials and solar cells, Small Methods 2 (1) (2018) 1700295.

[35] L.K. Ono, Y. Qi, Surface and interface aspects of organometal halide perovskite materials and solar cells, J. Phys. Chem. Lett. 7 (22) (2016) 4764–4794.

[36] H.J. Snaith, A. Abate, J.M. Ball, G.E. Eperon, T. Leijtens, N.K. Noel, S.D. Stranks, J.T.-W. Wang, K. Wojciechowski, W. Zhang, Anomalous hysteresis in perovskite solar cells, J. Phys. Chem. Lett. 5 (9) (2014) 1511–1515.

[37] W. Tress, N. Marinova, T. Moehl, S.M. Zakeeruddin, M.K. Nazeeruddin, M. Grätzel, Understanding the rate-dependent J–Vs hysteresis, slow time component, and aging in $CH_3NH_3PbI_3$ perovskite solar cells: the role of a compensated electric field, Energy Environ. Sci. 8 (2015) 995–1004.

[38] H. Tsai, R. Asadpour, J.-C. Blancon, C.C. Stoumpos, O. Durand, J.W. Strzalka, B. Chen, R. Verduzco, P.M. Ajayan, S. Tretiak, J. Even, M.A. Alam, M.G. Kanatzidis, W. Nie, A.D. Mohite, Light-induced lattice expansion leads to high-efficiency perovskite solar cells, Science 360 (6384) (2018) 67–70.

[39] J. Wei, Y. Zhao, H. Li, G. Li, J. Pan, D. Xu, Q. Zhao, D. Yu, Hysteresis analysis based on the ferroelectric effect in hybrid perovskite solar cells, J. Phys. Chem. Lett. 5 (21) (2014) 3937–3945.

[40] Y. Li, M. Behtash, J. Wong, K. Yang, Enhancing ferroelectric dipole ordering in organic–inorganic hybrid perovskite $CH_3NH_3PbI_3$: strain and doping engineering, J. Phys. Chem. C 122 (1) (2018) 177–184.

[41] S. Chen, X. Zhang, J. Zhao, Y. Zhang, G. Kong, Q. Li, N. Li, Y. Yu, N. Xu, J. Zhang, K. Liu, Q. Zhao, J. Cao, J. Feng, X. Li, J. Qi, D. Yu, J. Li, P. Gao, Atomic scale insights into structure instability and decomposition pathway of methylammonium lead iodide perovskite, Nat. Commun. 9 (1) (2018) 4807.

[42] K. Leng, I. Abdelwahab, I. Verzhbitskiy, M. Telychko, L. Chu, W. Fu, X. Chi, N. Guo, Z. Chen, Z. Chen, C. Zhang, Q.-H. Xu, J. Lu, M. Chhowalla, G. Eda, K.P. Loh, Molecularly thin two-dimensional hybrid perovskites with tunable optoelectronic properties due to reversible surface relaxation, Nat. Mater. 17 (10) (2018) 908–914.

[43] R. Ohmann, L.K. Ono, H.-S. Kim, H. Lin, M.V. Lee, Y. Li, N.-G. Park, Y. Qi, Real-space imaging of the atomic structure of organic–inorganic perovskite, J. Am. Chem. Soc. 137 (51) (2015) 16049–16054.

[44] C.C. Boyd, R. Cheacharoen, T. Leijtens, M.D. McGehee, Understanding degradation mechanisms and improving stability of perovskite photovoltaics, Chem. Rev. 119 (5) (2019) 3418–3451.

[45] D. Zhang, Y. Zhu, L. Liu, X. Ying, C.-E. Hsiung, R. Sougrat, K. Li, Y. Han, Atomic-resolution transmission electron microscopy of electron beamsensitive crystalline materials, Science 359 (6376) (2018) 675–679.

[46] H.-C. Hsu, B.-C. Huang, S.-C. Chin, C.-R. Hsing, D.-L. Nguyen, M. Schnedler, R. Sankar, R.E. Dunin-Borkowski, C.-M. Wei, C.-W. Chen, P. Ebert, Y.-P. Chiu,

Photodriven dipole reordering: key to carrier separa- tion in metalorganic halide perovskites, ACS Nano 13 (4) (2019) 4402–4409.

[47] L. She, M. Liu, D. Zhong, Atomic structures of $CH_3NH_3PBi_3$ (001) surfaces, ACS Nano 10 (1) (2016) 1126–1131.

[48] B.-S. Kim, M.-H. Choi, M.-S. Choi, J.-J. Kim, Composition-controlled organometal halide perovskite via ch3nh3i pressure in a vacuum co- deposition process, J. Mater. Chem. 4 (2016) 5663–5668.

[49] L. She, M. Liu, X. Li, Z. Cai, D. Zhong, Growth and interfacial structure of methylammonium lead iodide thin films on au(111), Surf. Sci. 656 (2017) 17–23.

[50] Y. Liu, K. Palotas, X. Yuan, T. Hou, H. Lin, Y. Li, S.-T. Lee, Atomistic origins of surface defects in $CH_3NH_3PbBr_3$ perovskite and their electronic structures, ACS Nano 11 (2) (2017) 2060–2065.

[51] A.M.A. Leguy, J.M. Frost, A.P. McMahon, V.G. Sakai, W. Kockelmann, C. Law, X. Li, F. Foglia, A. Walsh, B.C. O'Regan, J. Nelson, J.T. Cabral, P.R.F. Barnes, The dynamics of methylammonium ions in hybrid organic– inorganic perovskite solar cells, Nat. Commun. 6 (2015) 7124.

[52] M.T. Weller, O.J. Weber, P.F. Henry, A.M. Di Pumpo, T.C. Hansen, Complete structure and cation orientation in the perovskite photovoltaic methylammonium lead iodide between 100 and 352 K, Chem. Commun. 51 (2015) 4180–4183.

[53] M.-C. Shih, S.-S. Li, C.-H. Hsieh, Y.-C. Wang, H.-D. Yang, Y.-P. Chiu, C.-S. Chang, C.-W. Chen, Spatially resolved imaging on photocarrier generations and band alignments at perovskite/PbI_2 heterointerfaces of perovskite solar cells by light-modulated scanning tunneling microscopy, Nano Lett. 17 (2) (2017) 1154–1160.

[54] A.K. Guria, S.K. Dutta, S. Das Adhikari, N. Pradhan, Doping Mn^{2+} in lead halide perovskite nanocrystals: successes and challenges, ACS Energy Lett. 2 (5) (2017) 1014–1021.

[55] W. Liu, Q. Lin, H. Li, K. Wu, I. Robel, J.M. Pietryga, V.I. Klimov, Mn^{2+}-doped lead halide perovskite nanocrystals with dual-color emission controlled by halide content, J. Am. Chem. Soc. 138 (45) (2016) 14954–14961.

[56] D. Parobek, B.J. Roman, Y. Dong, H. Jin, E. Lee, M. Sheldon, D.H. Son, Exciton-to-dopant energy transfer in mn-doped cesium lead halide perovskite nanocrystals, Nano Lett. 16 (12) (2016) 7376–7380.

[57] Y. Zhou, Z.-J. Yong, K.-C. Zhang, B.-M. Liu, Z.-W. Wang, J.-S. Hou, Y.-Z. Fang, Y. Zhou, H.-T. Sun, B. Song, Ultrabroad photoluminescence and 11 electroluminescence at new wavelengths from doped organometal halide perovskites, J. Phys. Chem. Lett. 7 (14) (2016) 2735–2741.

[58] J. Hieulle, X. Wang, C. Stecker, D.-Y. Son, L. Qiu, R. Ohmann, L.K. Ono, A. Mugarza, Y. Yan, Y. Qi, Unraveling the impact of halide mixing on perovskite stability, J. Am. Chem. Soc. 141 (8) (2019) 3515–3523.

[59] B. Murali, S. Dey, A.L. Abdelhady, W. Peng, E. Alarousu, A.R. Kirmani, N. Cho, S.P. Sarmah, M.R. Parida, M.I. Saidaminov, A.A. Zhumekenov, J. Sun, M.S. Alias, E. Yengel, B.S. Ooi, A. Amassian, O.M. Bakr, O.F. Mohammed, Surface restructuring of hybrid perovskite crystals, ACS Energy Lett. 1 (6) (2016) 1119–1126.

[60] H. Tsai, W. Nie, J.-C. Blancon, C.C. Stoumpos, R. Asadpour, B. Harutyunyan, A.J. Neukirch, R. Verduzco, J.J. Crochet, S. Tretiak, L. Pedesseau, J. Even, M.A. Alam, G. Gupta, J. Lou, P.M. Ajayan, M.J. Bedzyk, M.G. Kanatzidis, A.D. Mohite, High-efficiency two-dimensional Ruddlesden–Popper perovskite solar cells, Nature 536 (2016) 312.

[61] C. Katan, N. Mercier, J. Even, Quantum and dielectric confinement effects in lower-dimensional hybrid perovskite semiconductors, Chem. Rev. 119 (5) (2019) 3140–3192.

[62] L. Gross, Recent advances in submolecular resolution with scanning probe microscopy, Nat. Chem. 3 (2011) 273.

[63] H. Mönig, Quantitative assessment of intermolecular interactions by atomic force microscopy imaging using copper oxide tips, Nat. Nanotechnol. 13 (2018) 371–375.

[64] F. Monn, Imaging the charge distribution within a single molecule, Nat. Nanotechnol. 7 (4) (2012) 223–231.